

# Optical Engineering

OpticalEngineering.SPIEDigitalLibrary.org

## Digital field of view correction combined dual-view transport of intensity equation method for real-time quantitative imaging

Qingtao Gong  
Qi Wei  
Jing Xu  
Yan Kong  
Zhilong Jiang  
Weiying Qian  
Yueyue Zhu  
Liang Xue  
Fei Liu  
Cheng Liu  
Shouyu Wang

Qingtao Gong, Qi Wei, Jing Xu, Yan Kong, Zhilong Jiang, Weiying Qian, Yueyue Zhu, Liang Xue, Fei Liu, Cheng Liu, Shouyu Wang, "Digital field of view correction combined dual-view transport of intensity equation method for real-time quantitative imaging," *Opt. Eng.* **57**(6), 063102 (2018), doi: 10.1117/1.OE.57.6.063102.

**SPIE**®

# Digital field of view correction combined dual-view transport of intensity equation method for real-time quantitative imaging

Qingtao Gong,<sup>a</sup> Qi Wei,<sup>a</sup> Jing Xu,<sup>a</sup> Yan Kong,<sup>a</sup> Zhilong Jiang,<sup>a</sup> Weiyang Qian,<sup>a</sup> Yueyue Zhu,<sup>b</sup> Liang Xue,<sup>b</sup> Fei Liu,<sup>c,d</sup> Cheng Liu,<sup>a,e,\*</sup> and Shouyu Wang<sup>a,d,\*</sup>

<sup>a</sup>Jiangnan University, School of Science, Computational Optics Laboratory, Wuxi, China

<sup>b</sup>Shanghai University of Electric Power, College of Electronics and Information Engineering, Shanghai, China

<sup>c</sup>Nanjing Agricultural University, Joint International Research Laboratory of Animal Health and Food Safety of Minster of Education, Nanjing, Jiangsu, China.

<sup>d</sup>Nanjing Agricultural University, Single Molecule Nanometry Laboratory, Nanjing, Jiangsu, China

<sup>e</sup>Chinese Academy of Sciences, Shanghai Institute of Optics and Fine Mechanics, Shanghai, China

**Abstract.** Dual-view transport of intensity equation (TIE) method is an ideal way for quantitative live cell imaging as it has advantages such as real-time imaging, multimode observations, compact setup, and large field of view (FoV). However, due to the image recorder installation error, the inevitable FoV mismatch between the captured under- and over-focus intensities reduces the accuracy in both amplitude and phase retrievals. Here, to eliminate this undesired FoV mismatch, the phase correlation-based digital FoV correction is adopted to recognize and compensate the rotation, scale, and translation between the under- and over-focus images. Both the numerical simulations as well as the experiments in standard sample detection and quantitative live cell imaging prove that the digital FoV correction combined dual-view TIE method can maintain the consistence of the dual FoVs, thus guaranteeing the high-accurate amplitude and phase computations, proving the proposed method is a promising quantitative live cell imaging tool in various applications such as biological observations and medical diagnostics. © 2018 Society of Photo-Optical Instrumentation Engineers (SPIE) [DOI: [10.1117/1.OE.57.6.063102](https://doi.org/10.1117/1.OE.57.6.063102)]

Keywords: computational imaging; phase measurement; microscopy.

Paper 180265 received Feb. 17, 2018; accepted for publication May 18, 2018; published online Jun. 5, 2018.

## 1 Introduction

Live cell imaging is an important tool for cellular observing and monitoring, and it is widely used in the biological and medical fields such as cellular dynamic measurements and condition evaluations. As most of the live cells are nearly transparent due to their low absorption and scattering, chemical staining and fluorescent labeling are often used to enhance the image contrast.<sup>1</sup> Unfortunately, these additional procedures not only complicate the sample preparations, but also affect the cellular functions. Compared with the widely used intensity-based microscopy, the label-free quantitative phase microscopy is a more appropriate approach especially for live cell imaging,<sup>2</sup> because the contrast of the obtained phase image is at least an order of magnitude higher than that of the intensity distribution; additionally, compared with the classical intensity-based imaging, quantitative phase imaging can reflect specimen details in a different perspective.<sup>3</sup> Therefore, various quantitative imaging techniques have been developed, acting as promising tools for live cell imaging.

Ptychography including spatial-domain iteration-based ptychographic iterative engine and frequency-domain iteration-based Fourier ptychographic microscopy is a classical technique for quantitative imaging.<sup>4–9</sup> However, the necessary multiple captures in data collections and the required

iterations in phase retrieval are time-consuming, indicating that ptychography is not the appropriate choice for live cell imaging. Interference-based quantitative interferometric microscopy and digital holographic microscopy can extract both the sample amplitude and phase information from a single-shot captured hologram,<sup>10–15</sup> thus they become widespread tools in real-time live cell imaging. However, in these methods, an extra reference beam is often required, thus complicating the experimental setup. In addition, both the ptychography and the interference approaches can be hardly integrated with the widely adopted commercial microscopes, limiting their potential applications in biological and medical fields.

To realize quantitative imaging based on commercial microscopes, a noninterference method through solving the transport of intensity equation (TIE) has been proposed.<sup>16–26</sup> Its optical system is compact and it does not need time-consuming phase retrieval processing. Unfortunately, traditional TIE methods require sample or image recorder translation for multifocal intensity captures, and the commonly used mechanical translation limits its applications in live cell imaging due to its low scanning speed. To accelerate the image recording speed, tunable lens was adopted for high-speed multifocal image recording, though its temporal resolution was remarkably increased compared with those based on mechanical translation,<sup>27,28</sup> it still cannot realize real-time

\*Address all correspondence to: Cheng Liu, E-mail: [cheng.liu@hotmail.co.uk](mailto:cheng.liu@hotmail.co.uk); Shouyu Wang, E-mail: [wsy\\_photonics@yahoo.com](mailto:wsy_photonics@yahoo.com)

measurements. Waller's group achieved real time under-, in-, and over-focus intensities relying on the chromatic aberrations in the imaging system;<sup>26</sup> however, it only works well when the samples are with low dispersion. In addition, Yu et al.<sup>29</sup> and Yang et al.,<sup>30</sup> respectively, designed single-shot TIE techniques by field of view (FoV) division, though these methods are potential for quantitative live cell imaging, they can only monitor small amount of cells due to the limited FoV. To break through the FoV restriction, Dai's group designed a beam-splitting system for simultaneous multifocal image captures using multiple cameras.<sup>23</sup> In addition, we also designed a dual-view TIE method:<sup>31</sup> two identical cameras were set at the binocular tubes to simultaneously capture the over- and under-focus images, and then both the cellular amplitude and phase can be computed according to the TIE method. This dual-view TIE method can realize real-time quantitative imaging with large FoV only with simple setup, proving that it especially suits for commercial microscope-based quantitative live cell imaging.

However, due to the rotation, translation, and even scale between the two captured under- and over-focus intensities, the FoV mismatch generates inevitably, and the accuracy is reduced in the amplitude and phase retrievals when using this dual-view TIE method. Unfortunately, the FoV mismatch can hardly be avoided experimentally by image recorder adjustments or system optimization. Here, to maintain the FoV consistency for high-accurate quantitative imaging, the classical phase correlation<sup>32</sup>-based digital FoV correction is adopted, which can recognize the rotation, scale, and translation between the under- and over-focus FoVs and correct them numerically in high precision. Both the numerical simulations as well as the experiments in both standard samples and live cells are provided to prove that the digital FoV correction-combined dual-view TIE method can obtain the accurate quantitative amplitude and phase imaging in real time avoiding the error caused by the FoV inconsistency, indicating that the digital FoV correction-combined dual-view TIE method is a promising tool for quantitative live cell imaging in biological research and medical diagnostics.

## 2 Principle of the Digital FoV Correction-Combined Dual-View TIE Method

Figure 1 shows the flowchart of the proposed digital FoV correction-combined dual-view TIE method. Figure 1(a) shows the optical system, which relies on the same two image recorders (CCD cameras, AVT Prosilica GC780, Germany) setting at the binocular tubes of a commercial microscope (ML-12, Mshot, China). With the C-mount brass spacer rings (Edmund Optics) shown in the inset of Fig. 1(a), these image recorders were located at different image planes aiming at capturing the under- and over-focus intensities. To guarantee the high-accurate phase retrieval, interference filters with working wavelengths of 532 nm (for random phase plate testing) and 632 nm (for cell imaging) both with full width at half maximum (FWHM) of 10 nm (Daheng Optics, China) were used in different cases for increasing the partially temporal coherence of the illumination light. In addition, Kohler illumination was implemented, and the condenser aperture was set as ~40% of the objective aperture to ensure the partially spatial coherent illumination.<sup>33–35</sup>

Before quantitative live cell imaging, the position of the sample stage should be adjusted. First, using the precision translation stage (MS-300, Mshot, China), massive images were captured by both the image recorders via the sample stage scanning along the optical axis. Next, the in-focus location of each image recorder can be determined according to the image gradient. Finally, the sample stage was moved to the center of these two determined in-focus positions, explaining that the two image recorders were able to simultaneously capture the under- and over-focus intensities as shown in Fig. 1(b), respectively.

Unfortunately, due to the improper installation of the two image recorders, FoV mismatch caused by rotation, scale, and translation was introduced as shown in Fig. 1(b), making it impossible for high-accurate quantitative imaging. Therefore, the mismatch needs to be compensated to keep the consistency between the under- and over-focus intensities

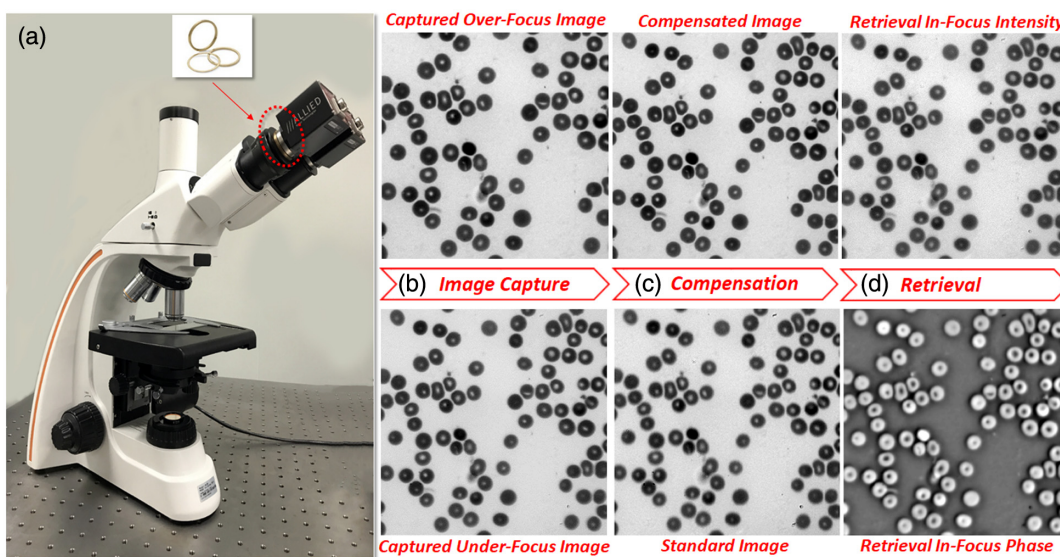


**Fig. 1** Flowchart of the digital FoV correction-combined dual-view TIE method. (a) Experimental setup, (b) simultaneously captured under- and over-focus images, (c) FoV mismatch compensated under- and over-focus images, and (d) retrieved in-focus intensity and phase distributions.

before further intensity and phase extraction. In our previous work,<sup>31</sup> the FoV rotation was first manually corrected via image recorder rotating, and then the translation was digitally compensated via image process, but the scale was ignored in our previous work. However, the FoV mismatch can hardly be completely compensated via this rough processing, indicating that a simple and rapid FoV correction approach is still required in the dual-view TIE system for pursuing high-accurate quantitative amplitude and phase extraction.

Here, according to the classical phase correlation method, the digital FoV correction was provided for under- and over-focus FoV correction. Equation (1) shows the translation case, supposing  $I_1$  is the standard image, and  $I_2$  is the shifted one from  $I_1$ ,  $x$  and  $y$  are the spatial coordinates,  $\Delta x$  and  $\Delta y$  are the translations in the two orthogonal directions, respectively

$$I_2(x, y) = I_1(x - \Delta x, y - \Delta y). \quad (1)$$

Equation (2) is obtained by taking the Fourier transform ( $\mathcal{F}$ ) of both sides in Eq. (1) [ $F_1 = \mathcal{F}(I_1)$ ,  $F_2 = \mathcal{F}(I_2)$ ,  $u$  and  $v$  are the frequency coordinates].

$$F_2(u, v) = F_1(u, v)e^{-iu\Delta x - iv\Delta y}. \quad (2)$$

To compute the translation, the exponential component can be extracted according to Eq. (3), in which “\*” represents the conjugation. The position of the peak ( $\delta$ ) reveals the translation details ( $\Delta x$  and  $\Delta y$ ), and the amplitude of the peak indicates the similarity of the two images<sup>36,37</sup>

$$\delta(x + \Delta x, y + \Delta y) = \mathcal{F}^{-1}\left(\frac{F_1(u, v)F_2^*(u, v)}{|F_1(u, v)F_2^*(u, v)|}\right). \quad (3)$$

Note that there should be only one  $\delta$  function in the ideal cases of the same two images only with translations. In practical cases, due to the noises and the slight difference between the under- and over-focus images, the peak width broadens and its peak amplitude decreases. However, the peak position can still be determined by tracking the maximum value obtained by Eq. (3), which means by tracking the position of the maximum value, translation details ( $\Delta x$  and  $\Delta y$ ) can be extracted according to Eq. (4). Additionally, the phase correlation method can still work well in cases with noises and slight image distinctions

$$(\Delta x, \Delta y) = \arg \max \{\delta(x + \Delta x, y + \Delta y)\}. \quad (4)$$

In addition, to deal with the scale and rotation mismatches, coordinate transformation is required.<sup>38-41</sup> Equation (5) shows two images  $I_1$  and  $I_2$  with both scale ( $s$ ) and rotation ( $\theta$ ) between them, and  $x' = s \cdot x \cdot \cos \theta + s \cdot y \cdot \sin \theta - x_0$ ,  $y' = -s \cdot x \cdot \sin \theta + s \cdot y \cdot \cos \theta - y_0$ .  $x_0$  and  $y_0$  are the additional displacement in spatial coordinates.

$$I_2(x, y) = I_1(x', y'). \quad (5)$$

Similar to Eq. (2), Eq. (6) is obtained by taking the Fourier transform of both sides in Eq. (5)

$$\begin{aligned} F_2(u, v) &= \frac{1}{s} e^{-iux_0 - ivy_0} F_1(u/s \cos \theta \\ &\quad + v/s \sin \theta, -u/s \sin \theta + v/s \cos \theta). \end{aligned} \quad (6)$$

Equation (7) is obtained by taking the amplitudes (| |) of both sides in Eq. (6)

$$\begin{aligned} |F_2(u, v)| &= \frac{1}{|s|} |F_1(u/s \cos \theta + v/s \sin \theta, -u/s \sin \theta \\ &\quad + v/s \cos \theta)|. \end{aligned} \quad (7)$$

Then, Eq. (8) is derived by substituting  $u = r \cdot \cos \varphi$  and  $v = r \cdot \sin \varphi$  into Eq. (7)

$$\begin{aligned} |F_2(u, v)| &= \frac{1}{|s|} |F_1(r/s \cos \theta \cos \varphi \\ &\quad + r/s \sin \theta \sin \varphi, -r/s \sin \theta \cos \varphi \\ &\quad + r/s \cos \theta \sin \varphi)| \\ &= \frac{1}{|s|} |F_1[r/s \cos(\varphi - \theta), r/s \sin(\varphi - \theta)]|. \end{aligned} \quad (8)$$

Next, Eq. (9) is obtained by applying the transformation from Cartesian coordinates ( $u, v$ ) to polar coordinates ( $r, \varphi$ )

$$|F_2(r, \varphi)| = \frac{1}{|s|} |F_1(r/s, \varphi - \theta)|. \quad (9)$$

Taking the logarithm of  $r$  and  $r + s$  to convert the division into subtraction, Eq. (10) can be derived, which is similar to Eq. (1). According to the method indicated by Eqs. (2) and (3), the “translation” in  $|F_1|$  and  $|F_2|$  as  $\log s$  and  $\theta$  can be retrieved. Finally, according to the coordinate transformation, both the rotation and scale between  $I_1$  and  $I_2$  can be recovered<sup>38-41</sup>

$$|F_2(\log r, \varphi)| = \frac{1}{|s|} |F_1(\log r - \log s, \varphi - \theta)|. \quad (10)$$

Figure 2 shows the pseudocode of the digital FoV correction method. Considering the relatively small defocus amount, both the under- and over-focus images are often treated as the similar images, but one of them is often scaled, rotated, and shifted due to the improper image recorder installation. According to the procedures listed in Fig. 2, the under-focus image was regarded as the standard image, and combining with the coordinate transformation, both the rotation and the scale in the over-focus image were first extracted, then after rotation and scale compensation, the translation was finally recognized and corrected as shown in Fig. 1(c). As the FoV mismatch was compensated after the digital correction, the in-focus intensity in Fig. 1(d) could be computed as the average of the under-focus and compensated over-focus intensities, and then the quantitative phase in Fig. 1(d) was extracted from multifocal images by solving the Poisson equation with the classical Fourier transform-based approach.<sup>42-44</sup> It is worth noting that both scale and rotation are first compensated and then the translation is corrected according to the proposed procedure; however, even changing the mismatch compensation order, precise FoV correction can still be realized. It is found that during the

<p><b>Input:</b> Over-Focus <math>O(x,y)</math> and Under-Focus <math>U(x,y)</math> images</p> <p><b>Step 1:</b> Scale &amp; Rotation Recognition and Compensation</p> <p>% Take the Fourier transform (<math>\mathcal{F}\{\cdot\}</math>) to the images</p> $O(u,v) = \mathcal{F}\{O(x,y)\} \quad U(u,v) = \mathcal{F}\{U(x,y)\}$ <p>% Extract the magnitude of <math>O(u,v)</math> and <math>U(u,v)</math></p> $O_a(u,v) = \text{abs}(O(u,v)) \quad U_a(u,v) = \text{abs}(U(u,v))$ <p>% Process with high passed filter to reduce edge effect</p> $O_a(u,v) = \text{HighPass}(u,v) * O_a(u,v)$ $U_a(u,v) = \text{HighPass}(u,v) * U_a(u,v)$ <p>% Transform <math>O_a(u,v)</math> and <math>U_a(u,v)</math> to log-polar coordinates</p> $r = \sqrt{u^2 + v^2} \quad \theta = \arctan(v/u)$ $O_a(\log r, \theta) = \text{LogPolar}\{O_a(u,v)\}$ $U_a(\log r, \theta) = \text{LogPolar}\{U_a(u,v)\}$ <p>% Take Fourier transform on <math>O_a(\log r, \theta)</math> and <math>U_a(\log r, \theta)</math></p> $O_A(k_u, k_v) = \mathcal{F}\{O_a(\log r, \theta)\}$ $U_A(k_u, k_v) = \mathcal{F}\{U_a(\log r, \theta)\}$ <p>% Compute cross power spectrum of <math>O_A</math> and <math>U_A</math></p> $\text{CrossPower}_1(k_u, k_v) = \frac{O_A(k_u, k_v) * \text{conj}\{U_A(k_u, k_v)\}}{ O_A(k_u, k_v) * \text{conj}\{U_A(k_u, k_v)\} }$	<p>% Take inverse Fourier transform, then Find the peak in the cross power distribution</p> $\{\log r_{\max}, \theta_{\max}\} = \max\{\mathcal{F}^{-1}\{\text{CrossPower}_1(k_u, k_v)\}\}$ <p><b>Output:</b> scale = <math>r_{\max}</math>, rotation = <math>\theta_{\max}</math></p> <p>% Compensate the captured images</p> $O'(x,y) = \text{Compensate}(O(x,y))$ $U'(x,y) = \text{Compensate}(U(x,y))$ <p><b>Step 2:</b> Translation Recognition and Compensation</p> <p>% Take the Fourier transform to the compensated images</p> $G_O(u,v) = \mathcal{F}\{O'(x,y)\} \quad G_U(u,v) = \mathcal{F}\{U'(x,y)\}$ <p>% Compute cross power spectrum of <math>G_O</math> and <math>G_U</math></p> $\text{CrossPower}_2(u,v) = \frac{G_O(u,v) * \text{conj}\{G_U(u,v)\}}{ G_O(u,v) * \text{conj}\{G_U(u,v)\} }$ <p>% Take inverse Fourier transform, then Find the peak in the cross power distribution</p> $\{x_{\max}, y_{\max}\} = \max\{\mathcal{F}^{-1}\{\text{CrossPower}_2(u,v)\}\}$ <p><b>Output:</b> <math>x_{\max}, y_{\max}</math> as the translation deviation</p> <p>% Retrieve the compensated images</p> $O(x,y) = \text{Compensate}(O'(x,y))$ $U(x,y) = \text{Compensate}(U'(x,y))$
--	--

**Fig. 2** Pseudocode of the digital FoV correction method.

scale and rotation corrections, there will be extra translation occurring. Therefore, if applying the processing order as first translation and then scale-rotation during the digital FoV correction, extra translation compensation is required, which obviously reduces the processing efficiency. Considering the processing speed, the order as first compensating rotation and scale and then correcting translation is preferred in this digital FoV correction method.

The adopted technique can digitally correct the inconsistent under- and over-focus images avoiding the time-consuming and complicated image recorder adjustments. Additionally, the processing speed of the digital FoV correction is rapid, as no procedure with massive computation is required. Using a computational platform with the Intel Core i5-3470 of 3.2 GHz and the RAM of 8 GB, it took 0.25 s to extract the FoV mismatch, and 0.16 s to realize FoV correction and 0.07 s to retrieve phase distribution according to the TIE method for images with  $512 \times 512$  pixels. It is worth noting that the mismatch recognition can be implemented using a standard sample before quantitative live cell imaging. To simultaneously record, process, and show the dynamics of the live cells, around 0.23 s was required. Moreover, using computational platform with faster processing speed or decreasing the recording pixel sizes, the frame rate can even be raised for future real-time live cell imaging. Here in this work, we first captured both the under- and over-focus images with rather high frame rate (20 fps), and after image recording, the quantitative imaging processing including digital FoV correction and TIE phase retrieval was then

implemented to extract the cell dynamics. In this way, cell dynamics can be recorded in rather high frequency, however, partially sacrificing the real-time computation and cellular dynamic showing. Moreover, the digital FoV correction can be either implemented before sample imaging using a standard sample, or used directly during the measurements, indicating that the added digital FoV correction will not restrict the real-time quantitative imaging when using the dual-view TIE method. However, in the processing for digital FoV correction, the error-prone coordinate transformation and logarithmic calculation are required, in addition, there is still slight difference between the under- and over-focus images, mistakes might be introduced in FoV mismatch recognition and compensation; therefore, before practical measurements, numerical simulations are provided to check the accuracy of the digital FoV correction.

### 3 Numerical Simulations

To evaluate the performance of the digital FoV correction-combined dual-view TIE method, numerical simulations were first implemented, in which the parameters such as the pixel size of the image recorders as  $7.4 \mu\text{m}$ , the defocus distance as 1.50 mm, and the illumination wavelength as 532 nm were all in accordance with the experimental devices.

Figures 3(a) and 3(b) show the setting amplitude and phase, and Figs. 3(c) and 3(d), respectively, show that the under- and over-focus intensities that are both 1.50 mm away from the focal plane numerically computed via the

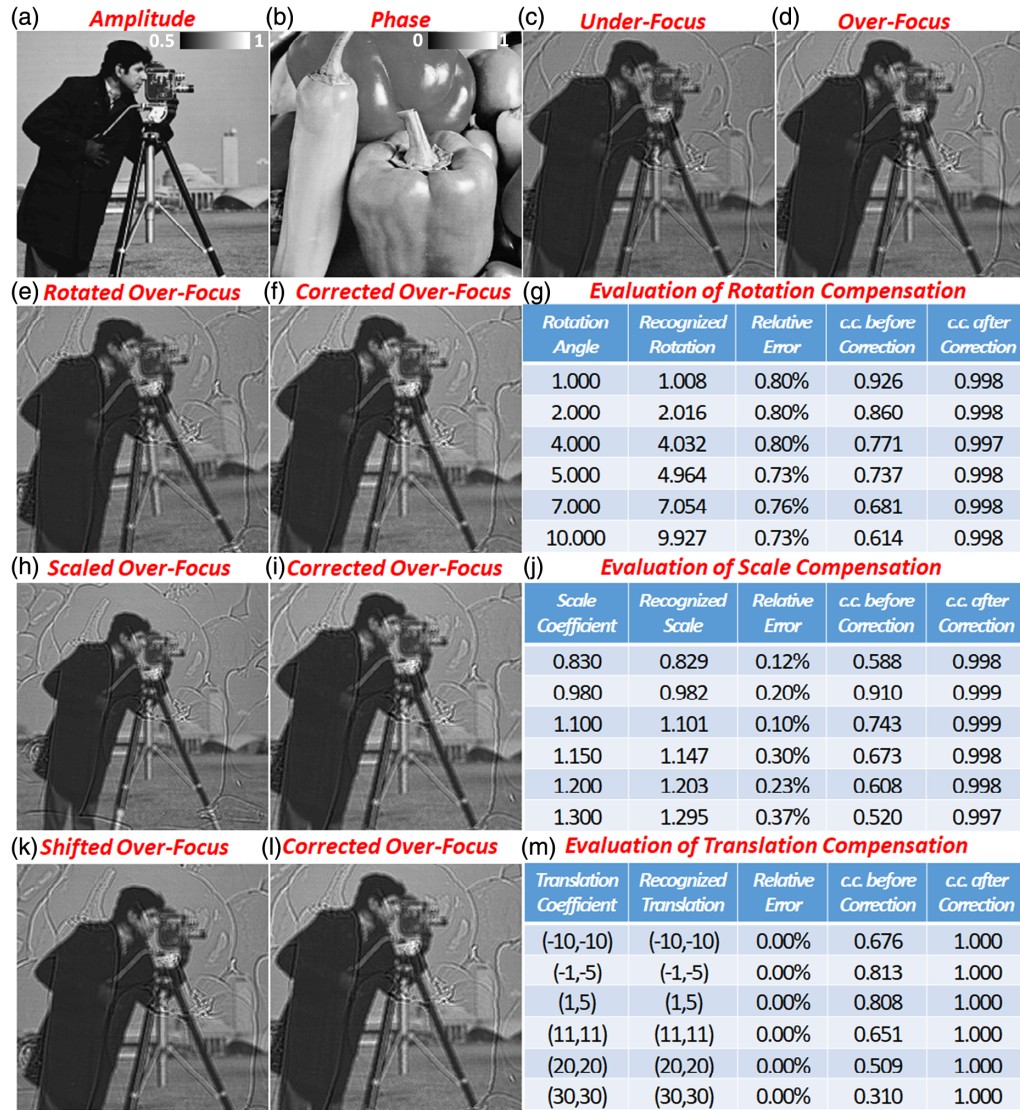


**Fig. 3** Numerical simulations of the digital FoV correction method. (a) and (b) Preset amplitude and phase distributions, (c) and (d) numerically computed under- and over-focus images, (e) rotated over-focus image, (f) compensated over-focus image, (g) quantitative evaluation of the digital FoV correction in rotation compensation, (h) scaled over-focus image, (i) compensated over-focus image, (j) quantitative evaluation of the digital FoV correction in scale compensation, (k) shifted over-focus image, (l) compensated over-focus image, (m) quantitative evaluation of the digital FoV correction in translation compensation. c.c. in (g), (j), and (m) indicates correlation coefficients.

angular spectrum method.<sup>45</sup> In the numerical simulations, the under-focus image was regarded as the standard, whereas the pre-set errors as rotation, scale, and translation were first introduced into the over-focus one; next, using the digital FoV correction, the mismatch information was computed and the compensated over-focus image was obtained; finally, correlation computation was adopted to quantitatively evaluate the performance of the digital FoV correction.

First, digital FoV corrections on the separate error were quantitatively analyzed. Figure 3(e) is the rotated over-focus image with a rotation angle of 5.000 deg. Using the digital FoV correction, the rotation compensated over-focus image is shown in Fig. 3(f), and the recognized rotation angle was 4.964 deg, indicating an extremely low relative error as 0.730%. Moreover, the correlation coefficient between the original over-focus image in Fig. 3(d) and the rotated one in Fig. 3(e) was 0.737, whereas that between the original

one and the compensated one in Fig. 3(f) was 0.998, illustrating that the digital FoV correction can well compensate the FoV inconsistency. In addition, various conditions were also tested with different rotation angles from 1.000 deg to 10.000 deg listed in Fig. 3(g): the relative errors were always <1%, and the correlation coefficients between the original ones and the compensated ones were increased obviously compared with those between the original ones and the rotated ones, the simulation results proved that the digital FoV correction precisely compensated the rotation between the under- and over-focus images. Next, Fig. 3(h) shows a scale-down over-focus image with the scaling coefficient of 0.830, and Fig. 3(i) is the compensated one using the digital FoV correction, indicating a recognized scaling coefficient of 0.829 and the low relative error of 0.120%. In addition, Fig. 3(j) lists the performance of the digital FoV correction in different scaling conditions, the relatively

low-scale recognition error as well as the obvious increase in correlation coefficients after scale compensation proved the scale between the under- and over-focus images can be well recognized and compensated. Finally, Figs. 3(k) and 3(l) show the shifted over-focus image with 20 pixels upward and 20 pixels rightward and the precisely compensated result, respectively. The results listed in Fig. 3(m) explained that the translation between the dual FoV was recognized and compensated in extremely high precision. Therefore, according to the quantitative numerical simulation in Fig. 3, it is proved the digital FoV correction can well compensate the FoV mismatch induced by the separate rotation, scale, and translation errors.

To check the performance of the digital FoV correction in the actual cases often with the coexistence of rotation, scale, and translation between the under- and over-focus intensities, numerical simulations shown in Fig. 4 were implemented. Figures 4(a) and 4(b) are the under- and over-focus intensities numerically computed from the amplitude and the phase shown in Figs. 3(a) and 3(b). Similar to the simulations in Fig. 3, the under-focus image was still regarded as the standard one, and the rotation, scale, and translation errors were all introduced in the over-focus one. Figure 4(c) was a modulated over-focus image with the rotation angle of 5.000 deg, the scaling coefficient of 1.100, the translation of 5 pixels downward, and 5 pixels leftward; and Fig. 4(f) was another example with the rotation angle of 7.000 deg, the scaling coefficient of 1.200, the translation of 8 pixels downward, and 8 pixels leftward. The FoVs of the modulated over-focus images were obviously inconsistent with that of the over-focus one, which can also be quantitatively evaluated by the correlation computation: the correlation coefficient between Figs. 4(b) and 4(c) was 0.696, and that between Figs. 4(b) and 4(d) was 0.580, it is mentioned that the relatively low correlation coefficients indicated the

obvious FoV mismatch. Using the digital FoV correction, the compensated over-focus images are shown in Figs. 4(e) and 4(f), with the recognized rotation angles of 4.964 deg and 7.054 deg, the scale coefficients of 1.101 and 1.203, and the translation corrections as four pixels upward/32 pixels leftward and 56 pixels leftward, respectively, proving the accuracy of the mismatch corrections. (It is worth noting that during the scale and rotation corrections, extra translation is introduced; the final translation correction data are often different from the original setting, but the recognized rotation angles and scale coefficients are quite close to original setting ones.) In addition, the correlation coefficients between the compensated under-focus images [Figs. 4(e) and 4(f)] and the error free under-focus one in Fig. 4(b) were both 0.985 and 0.984, respectively. Moreover, Figs. 4(g) and 4(h) reveal the retrieved phases using the digital FoV correction combined dual-view TIE method, which can guarantee high accuracy in phase extraction: estimated by the correlation computation, the correlation coefficients between the retrieved phase and the original set ones were 0.964 and 0.954, respectively. Considering the precise FoV compensation and accurate phase retrieval, the numerical simulations certificate the digital FoV correction-combined dual-view TIE approach is a useful tool for quantitative live cell imaging in biological and medical applications.

#### 4 Experiments

Before applying the digital FoV correction-combined dual-view TIE method in quantitative live cell imaging, the performance of the digital FoV correction was certified experimentally. Figures 5(a) and 5(b) were the simultaneously captured under- and over-focus images of a 1951 USAF resolution target (Thorlabs), respectively. In addition the blur due to the defocus effect, there was obvious FoV mismatch induced by the improper image recorder

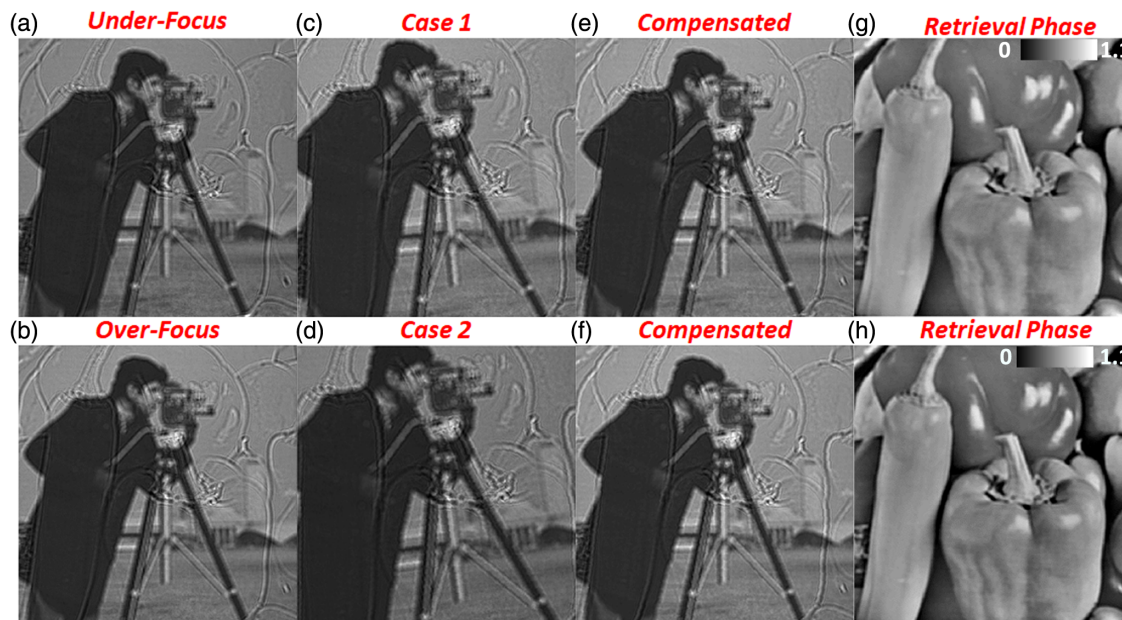


**Fig. 4** Numerical simulations of the digital FoV correction-based dual-view TIE method. (a) and (b) Numerically computed under- and over-focus images, (c) and (d) modulated over-focus images with different rotations, scaling, and translation, (e) and (f) compensated over-focus images using the digital FoV correction corresponding to (c) and (d), respectively, (g) and (h) retrieved phases in different cases.

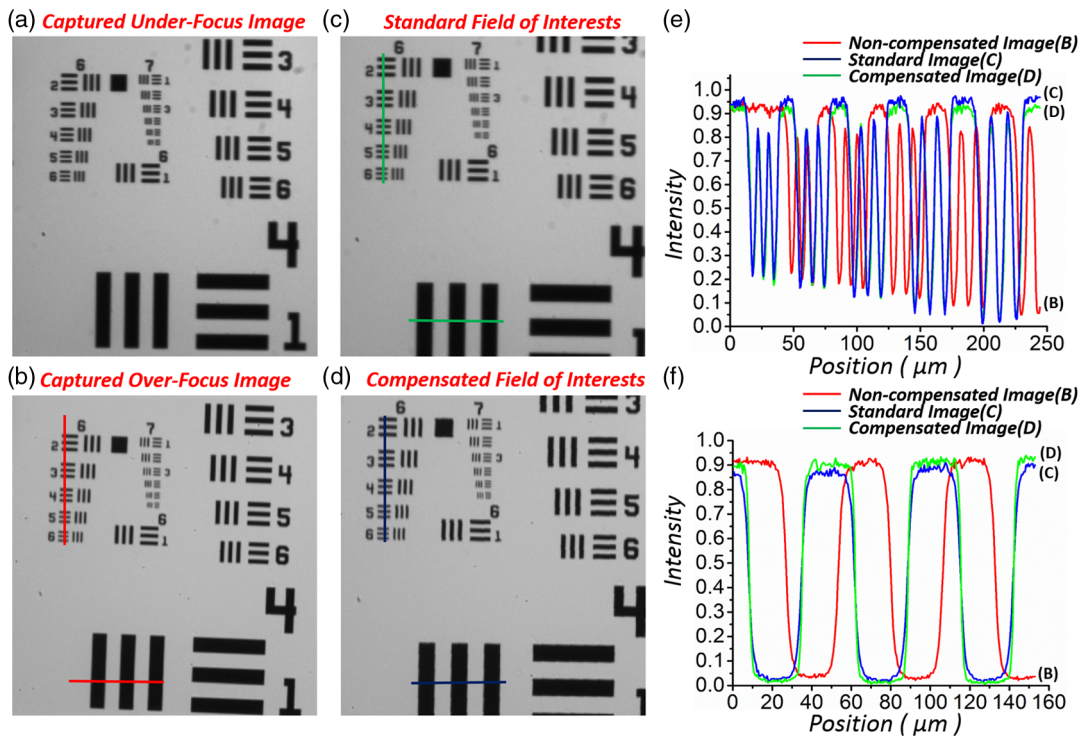


**Fig. 5** Experimental certification of the digital FoV correction. (a) and (b) Simultaneously captured under- and over-focus images of a 1951 USAF resolution target, (c) and (d) fields of interests of the standard under-focus image and the compensated over-focus image, (e) and (f) intensity comparisons along the lines in (b), (c), and (d).

installations. To compensate the FoV inconsistency, here, the under-focus image was regarded as the standard, whereas the over-focus one was processed using the digital FoV correction. Figures 5(c) and 5(d) reveal the fields of interests of the standard under-focus image and the compensated over-focus image, respectively, and the image consistency indicates that the FoV mismatch was well corrected. Moreover, to quantitatively check the performance of the digital FoV correction, Figs. 5(e) and 5(f) show the intensity distributions along the lines in Figs. 5(b)–5(d), respectively. According to the comparison, it shows that the additional digital FoV correction can well compensate the FoV mismatch, and the coincidence of intensity distributions along the lines in Figs. 5(c) and 5(d) proved that the digital FoV correction can precisely compensate the FoV mismatch, and thus supporting the high-accurate quantitative live cell imaging.

Combining with the digital FoV correction, the improved dual-view TIE method was adopted for quantitative imaging. First, a standard random phase plate (fabricated by Shanghai Institute of Optics and Fine Mechanics, Chinese Academy of Sciences) was used as a standard sample to certificate capability of the improved dual-view TIE method, as well as the accuracy of the optical system. There are only two phase steps with the phase difference of  $\pi$  at the wavelength of 633 nm. In the measurements, the illumination was obtained by an interference filter (Daheng Optics, China) with the central wavelength at 633 nm and the full width at half maximum of 10 nm. Figures 6(a) and 6(b) reveal the simultaneously captured under- and over-focus images using the dual-view TIE system, respectively, indicating there is obvious FoV mismatch between these two multifocal images. Next, Fig. 6(c) is the FoV compensated over-focus

image that is obtained via the proposed digital FoV correction method. Finally, the in-focus intensity was computed in Fig. 6(d) as the average of Figs. 6(a) and 6(c). Figure 6(e) shows the poor result of the retrieved phase from Figs. 6(a) and 6(b) without digital FoV correction. While using the proposed method, the quantitative phase distribution was computed by solving the TIE as shown in Fig. 6(f), indicating an obvious phase difference of  $\sim\pi$ . Moreover, traditional TIE approach based on sample translation was also implemented for imaging accuracy evaluation: the FoV was kept unchanged, and one CCD camera was still set at the binocular tube, then the sample stage was scanned along the optical axis to capture three under-, in-, and over-focus images for phase extraction, the sample phase shown in Fig. 6(g) was finally computed from these multifocal intensities. To quantitatively compare the phases obtained by different methods, Fig. 6(h) shows the phase comparison along the lines in Figs. 6(e)–6(g), the extracted phases in Figs. 6(f) and 6(g) coincide with each other well, illustrating that the digital FoV correction-combined improved dual-view TIE method can realize high-accurate quantitative imaging, moreover, according to the comparison between the lines in Figs. 6(e) and 6(f), it shows that the digital FoV correction can obviously improve the phase image quality, indicating that the digital FoV correction is essential for the dual-view TIE technique.

Next, quantitative images of biological cells were obtained using the digital FoV correction-combined dual-view TIE method. The used illumination wavelength was obtained by another interference filter (Daheng Optics, China) with the central wavelength at 532 nm and the full width at half maximum of 10 nm. Figure 7 shows the

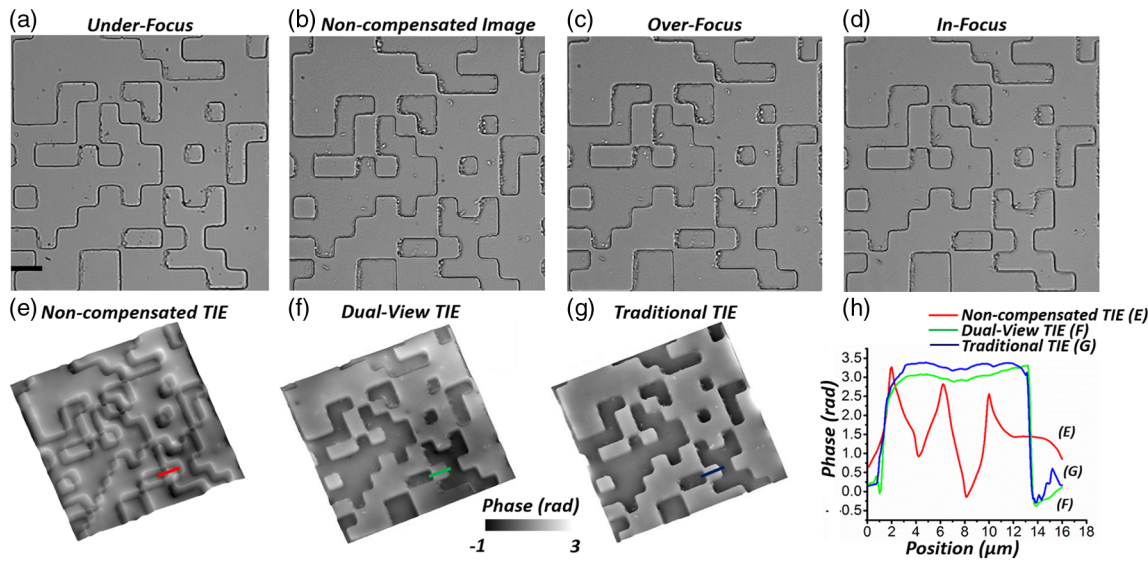


**Fig. 6** Measurements of standard random phase plate with the digital FoV correction-combined dual-view TIE method. (a) and (b) Simultaneously captured under- and over-focus images using the dual-view TIE system, (c) calculated over-focus intensity after FoV mismatch compensation, (d) calculated in-focus intensity after FoV mismatch compensation, (e) Retrieved phase using dual-view TIE method without digital FoV correction, (f) retrieved phase using dual-view TIE method with digital FoV correction, (g) retrieved phase using the traditional TIE method relying on sample scanning, (h) phase comparisons along the lines in (e), (f), and (g). Black bar in (a) indicates 20  $\mu\text{m}$ .

quantitative imaging results of a red blood cell slice (Keda Biological Sample Company, China). Figures 7(a) and 7(b) show the simultaneously captured under- and over-focus image; after FoV mismatch compensation, Figs. 7(c) and 7(d) are the reconstructed over-focus and in-focus intensities, respectively. Figures 7(e) and 7(f) are the reconstructed phase using the dual-view TIE without and with digital FoV correction, and Fig. 7(g) shows the phase retrieved using the traditional TIE based on sample scanning.

According to the quantitative comparison shown in Fig. 7(h), the phase obtained via the traditional TIE method and the dual-view TIE method with digital FoV correction coincides with each other well. In addition, considering the refractive index of the red blood cell and the paraffin wax as 1.41 and 1.42, respectively, the average maximum height of the red blood cells was  $\sim 2.42 \mu\text{m}$ , close to that of the red blood cell model obtained from statistical measurements from a large amount of specimen.<sup>46</sup> These results proved

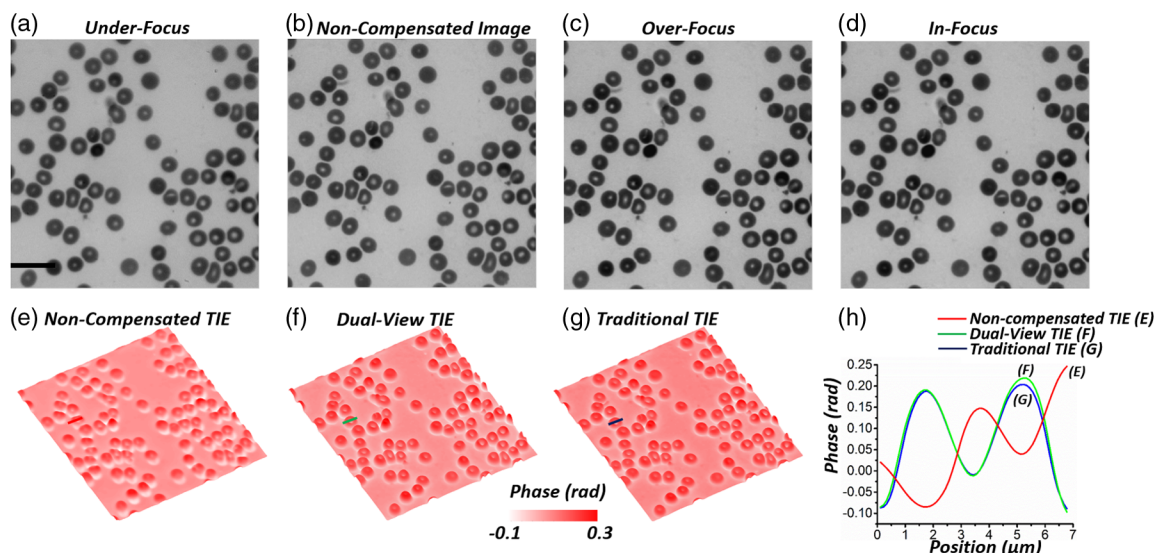


**Fig. 7** Measurements of red blood cells with the digital FoV correction-combined dual-view TIE method. (a) and (b) Simultaneously captured under- and over-focus images using the dual-view TIE system, (c) calculated over-focus intensity after FoV mismatch compensation, (d) calculated in-focus intensity after FoV mismatch compensation, (e) retrieved phase using dual-view TIE method without digital FoV correction, (f) retrieved phase using dual-view TIE method with digital FoV correction, (g) retrieved phase using the traditional TIE method relying on sample scanning, (h) phase comparisons along the lines in (e), (f), and (g). Black bar in (a) indicates 20  $\mu\text{m}$ .

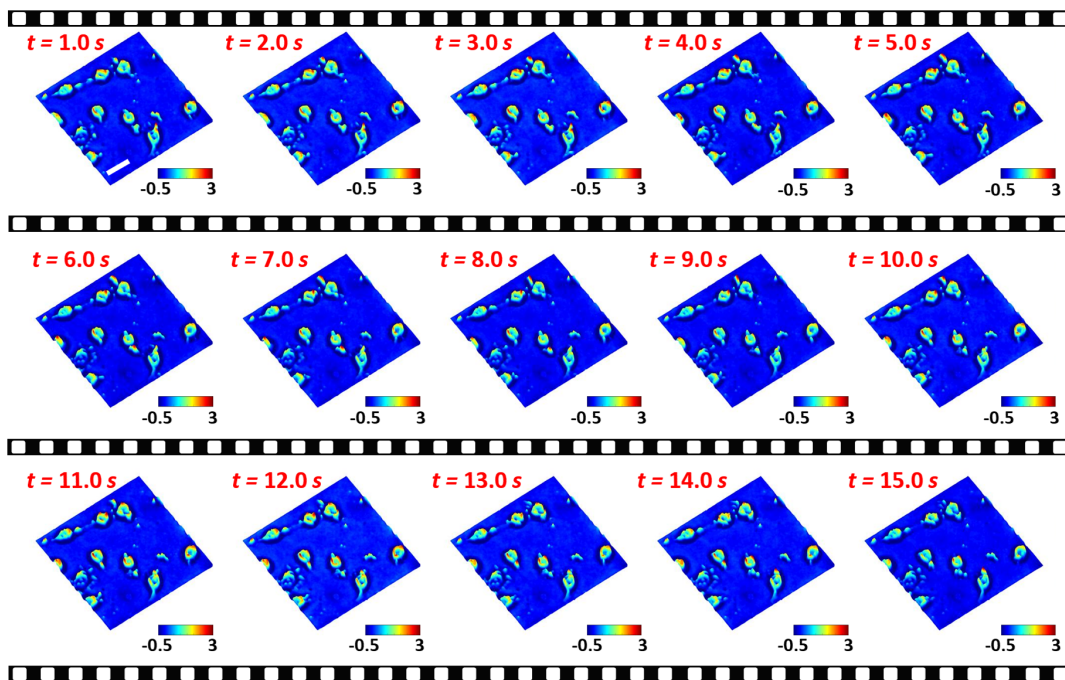


**Fig. 8** Phase dynamics (Video 1) retrieved by the digital FoV correction-combined dual-view TIE method. White bar indicates  $40 \mu\text{m}$ . (Video 1, MPEG, 2.7 MB [URL: <https://doi.org/10.1117/1.OE.57.6.063102.1>]).

the good performance of the digital FoV correction-combined dual-view TIE method in quantitative biological cell imaging.

Finally, live murine colon carcinoma cells were quantitatively observed using the digital FoV correction-combined dual-view TIE method. In the measurement, the used illumination wavelength was 532 nm, the capturing rates of both the CCD cameras were set as 20 fps, and their simultaneity was maintained using our self-built program. Figure 8 shows partial retrieved phases at different times during the observation period, and Video 1 reveals the whole phase fluctuation process. These results indicate that the cellular dynamics can be quantitatively measured and analyzed using the dual-view TIE method combining with the digital FoV correction. Considering the advantages as FoV mismatch compensation, large FoV, real-time measuring, and simple optical system, it is proved that the digital FoV correction-based dual-view TIE method is a promising tool in quantitative live cell imaging.

## 5 Conclusions

Dual-view TIE method is an appropriate method for tracking the live cell dynamics. However, it often suffers from the FoV mismatch due to the improper image recorder installation at the binocular of the microscopes, thus decreasing the accuracy in both intensity and phase retrievals. To compensate the FoV mismatch in the dual-view TIE approach, we have improved the dual-view TIE method combining with the digital FoV correction, which is used to distinguish and remove the rotation, scale, and translation between the simultaneously captured under- and over-focus intensities, thus both the amplitude and phase can be extracted in high accuracy. Numerical simulations and experimental resolution target certification proved that the adopted phase correlation

based digital FoV correction could distinguish and compensate the dual FoV mismatch with extremely high precision. Moreover, using the random phase plate, as well as the red blood cell slice, the accuracy of the digital FoV correction-combined dual-view TIE approach was certificated experimentally. Finally, according to the measurements on the dynamic live cells, it is proved that the digital FoV correction-combined dual-view TIE approach can be well adopted in quantitative live cell observations and measurements. Considering the advantages as real-time imaging, multimode observations, compact setup, and large FoV, it is believed the digital FoV correction-combined dual-view TIE approach is a promising tool for quantitative live cell imaging in both biological research and medical diagnostics.

## Disclosures

All the authors have no relevant financial interests in this article and no potential conflicts of interest to disclose.

## Acknowledgments

This research was supported by the Natural Science Foundation of China (61705092, U1730132, 31522056, and 11647144), the Natural Science Foundation of Jiangsu Province of China (BK20170194), Shanghai Sailing Program (17YF1407000), and Fundamental Research Funds for the Central Universities (JUSRP115A14 and JUSRP51721B).

## References

1. J. L. Schwartz and G. H. Patterson, "Development and use of fluorescent protein markers in living cells," *Science* **300**(5616), 87–91 (2003).
2. D. J. Stephens and V. J. Allan, "Light microscopy techniques for live cell imaging," *Science* **300**(5616), 82–86 (2003).
3. M. Mir et al., "Quantitative phase imaging," *Prog. Opt.* **57**, 133–217 (2012).

4. H. M. Faulkner and J. M. Rodenburg, "Movable aperture lensless transmission microscopy: a novel phase retrieval algorithm," *Phys. Rev. Lett.* **93**(2), 023903 (2004).
5. J. M. Rodenburg and H. M. L. Faulkner, "A phase retrieval algorithm for shifting illumination," *Appl. Phys. Lett.* **85**(20), 4795–4797 (2004).
6. G. Zheng, R. Horstmeyer, and C. Yang, "Wide-field, high-resolution Fourier ptychographic microscopy," *Nat. Photonics* **7**(9), 739–745 (2013).
7. L. Bian et al., "Content adaptive illumination for Fourier ptychography," *Opt. Lett.* **39**(23), 6648–6651 (2014).
8. W. Yu et al., "High-quality image reconstruction method for ptychography with partially coherent illumination," *Phys. Rev. B* **93**, 241105 (2016).
9. A. M. Maiden et al., "Soft x-ray spectromicroscopy using ptychography with randomly phased illumination," *Nat. Commun.* **4**, 1669 (2013).
10. A. Nativ and N. T. Shaked, "Compact interferometric module for full-field interferometric phase microscopy with low spatial coherence illumination," *Opt. Lett.* **42**(8), 1492–1495 (2017).
11. M. Shan, M. E. Kandel, and G. Popescu, "Refractive index variance of cells and tissues measured by quantitative phase imaging," *Opt. Express* **25**(2), 1573–1581 (2017).
12. M. Shan et al., "White-light diffraction phase microscopy at doubled space-bandwidth product," *Opt. Express* **24**(25), 29033–29039 (2016).
13. V. Bianco et al., "Optofluidic holographic microscopy with custom field of view (FoV) using a linear array detector," *Lab Chip* **15**(9), 2117–2124 (2015).
14. D. Hillmann et al., "Holoscopy: holographic optical coherence tomography," *Opt. Lett.* **36**(13), 2390–2392 (2011).
15. F. Merola et al., "Tomographic flow cytometry by digital holography," *Light Sci. Appl.* **6**(4), e16241 (2017).
16. G. Barbastathis et al., "Compressive x-ray phase tomography based on the transport of intensity equation," *Opt. Lett.* **38**(17), 3418–3421 (2013).
17. Y. Zhu et al., "Low-noise phase imaging by hybrid uniform and structured illumination transport of intensity equation," *Opt. Express* **22**(22), 26696–26711 (2014).
18. S. S. Gorthi and E. Schonbrun, "Phase imaging flow cytometry using a focus-stack collecting microscope," *Opt. Lett.* **37**(4), 707–709 (2012).
19. S. Shan et al., "Transport-of-intensity approach to differential interference contrast (TI-DIC) microscopy for quantitative phase imaging," *Opt. Lett.* **35**(3), 447–449 (2010).
20. L. G. Mesquita, U. Agero, and O. N. Mesquita, "Defocusing microscopy: an approach for red blood cell optics," *Appl. Phys. Lett.* **88**(13), 133901 (2006).
21. G. Glionna et al., "Tomography of fluctuating biological interfaces using defocusing microscopy," *Appl. Phys. Lett.* **94**(19), 193701 (2009).
22. P. M. S. Roma et al., "Total three-dimensional imaging of phase objects using defocusing microscopy: application to red blood cells," *Appl. Phys. Lett.* **104**(25), 251107 (2014).
23. C. Ma et al., "Transparent object reconstruction via coded transport of intensity," in *IEEE Conf. on Computer Vision and Pattern Recognition*, pp. 3238–3245 (2014).
24. B. Xue et al., "Transport of intensity phase imaging from multiple intensities measured in unequally-spaced planes," *Opt. Express* **19**(21), 20244–20250 (2011).
25. J. Zhong et al., "Transport of intensity phase imaging by intensity spectrum fitting of exponentially spaced defocus planes," *Opt. Express* **22**(9), 10661–10674 (2014).
26. L. Waller et al., "Phase from chromatic aberrations," *Opt. Express* **18**(22), 22817–22825 (2010).
27. C. Zuo et al., "High-speed transport-of-intensity phase microscopy with an electrically tunable lens," *Opt. Express* **21**(20), 24060–24075 (2013).
28. T. Nguyen et al., "Fully automated, high speed, tomographic phase object reconstruction using the transport of intensity equation in transmission and reflection configurations," *Appl. Opt.* **54**(35), 10443–10453 (2015).
29. W. Yu et al., "Real time quantitative phase microscopy based on single-shot transport of intensity equation (sstIE) method," *Appl. Phys. Lett.* **109**(7), 071112 (2016).
30. Z. Yang and Q. Zhan, "Single-shot smartphone-based quantitative phase imaging using a distorted grating," *PLoS One* **11**(7), e0159596 (2016).
31. X. Tian et al., "Real-time quantitative phase imaging based on transport of intensity equation with dual simultaneously recorded field of view," *Opt. Lett.* **41**(7), 1427–1430 (2016).
32. H. Foroosh, J. B. Zerubia, and M. Berthod, "Extension of phase correlation to subpixel registration," *IEEE Trans. Image Process.* **11**(3), 188–200 (2002).
33. E. D. Barone-Nugent, A. Barty, and K. A. Nugent, "Quantitative phase-amplitude microscopy I: optical microscopy," *J. Microsc.* **206**(3), 194–203 (2002).
34. C. J. Sheppard, "Defocused transfer function for a partially coherent microscope and application to phase retrieval," *J. Opt. Soc. Am. A* **21**(5), 828–831 (2004).
35. C. J. R. Sheppard, "Three-dimensional phase imaging with the intensity transport equation," *Appl. Opt.* **41**(28), 5951–5955 (2002).
36. H. S. Stone et al., "A fast direct fourier-based algorithm for subpixel registration of images," *IEEE Trans. Geosci. Remote Sens.* **39**(10), 2235–2243 (2001).
37. L. R. Benckert and M. Sjödahl, "Electronic speckle photography: analysis of an algorithm giving the displacement with subpixel accuracy," *Appl. Opt.* **32**(13), 2278–2284 (1993).
38. Q. S. Chen, M. Defrise, and F. Deconinck, "Symmetric phase-only matched filtering of Fourier–Mellin transforms for image registration and recognition," *IEEE Trans. Pattern Anal. Mach. Intell.* **16**(12), 1156–1168 (1994).
39. E. D. Castro and C. Morandi, "Registration of translated and rotated images using finite Fourier transforms," *IEEE Trans. Pattern Anal. Mach. Intell.* **PAMI-9**(5), 700–703 (1987).
40. B. S. Reddy and B. N. Chatterji, "An FFT-based technique for translation, rotation, and scale-invariant image registration," *IEEE Trans. Image Process.* **5**(8), 1266–1271 (1996).
41. F. Ghorbel, "Robust and efficient Fourier–Mellin transform approximations for gray-level image reconstruction and complete invariant description," *Comput. Vision Image Understanding* **83**(1), 57–78 (2001).
42. M. R. Teague, "Deterministic phase retrieval: a green's function solution," *J. Opt. Soc. Am.* **73**(11), 1434–1441 (1983).
43. A. Barty et al., "Quantitative optical phase microscopy," *Opt. Lett.* **23**(11), 817–819 (1998).
44. T. E. Gureyev and K. A. Nugent, "Rapid quantitative phase imaging using the transport of intensity equation," *Opt. Commun.* **133**(1), 339–346 (1997).
45. J. W. Goodman, *Introduction to Fourier Optics*, 3rd ed., Roberts and Company Publishers, Greenwood Village, Colorado (2004).
46. S. V. Tsinopoulos and D. Polyzos, "Scattering of He-Ne laser light by an average-sized red blood cell," *Appl. Opt.* **38**(25), 5499–5510 (1999).

Biographies for the authors are not available.